

# DNS and LES of a shear-free mixing layer

By B. Knaepen, O. Debligny<sup>†</sup> and D. Carati<sup>†</sup>

## 1. Introduction

The shear-free mixing layer represents one of the simplest inhomogeneous flows. It consists of two ‘distinct’ homogeneous regions of different turbulent kinetic energy interacting through a layer of rapid transition. The layer is said to be shear-free since the two homogeneous regions have no relative velocity. While flows encountered in nature or industrial applications are more often not devoid of shear, the study of the shear-free mixing layer is nevertheless useful since it allows the mixing properties of turbulence to be examined in a simplified environment. Indeed, turbulent transport properties in shear flows are more difficult to track since they can be overwhelmed by production sources originating from gradients in the mean velocity.

The shear-free mixing layer has already received attention in the past, both from the experimental and the numerical point of view. The first experimental study of the shear-free mixing layer is due to Glibert (1980). The flow was obtained by forcing a stream through a grid with two different mesh spacings. The two sides of the grid have however equal solidity resulting in an outgoing shear-free flow. In this first experimental study, the author mainly concentrated his attention on the downstream evolution of the spreading-rate parameter, which is a measure of the thickness of the mixing-layer. A more extensive experimental study was later performed by Veeravalli & Warhaft (1987, 1989). Owing to a different experimental setup, the authors achieved a higher ratio between the energies characterizing the two sides of the flow and this resulted in the observation of large-scale intermittency in the flow. The Veeravalli & Warhaft (1989) data will be used here as the main benchmark for the present study since it contains a detailed documentation of the flow characteristics we will be examining. From the numerical point of view, the shear-free mixing layer was studied in Briggs *et al.* (1996) using DNS. In that article the authors also used the data of Veeravalli & Warhaft (1989) as the point of comparison. Their simulations were done using a spectral code with a resolution of  $128^3$  Fourier modes. The microscale Reynolds numbers reached in the low- and high-energy homogeneous regions were, respectively, 11 and 22.5, which are roughly half of the values reported in the Veeravalli & Warhaft (1989) experiment (note that Briggs *et al.* (1996) use a different definition of the microscale Reynolds number than the one in Veeravalli & Warhaft (1989) and here). However, when properly nondimensionalized, they were able to reproduce satisfactorily the turbulence statistics of the flow.

The purpose of this work is twofold. First, given the computational resources available today, it is possible to reach, using DNS, higher Reynolds numbers than in Briggs *et al.* (1996). In the present study, the microscale Reynolds numbers reached in the low- and high-energy homogeneous regions are, respectively, 32 and 69. The results reported earlier can thus be complemented and their robustness in the presence of increased turbulence studied. The second aim of this work is to perform a detailed and documented LES of

<sup>†</sup> Université Libre de Bruxelles, Statistical and Plasma Physics, CP231, Boulevard du Triomphe, Campus Plaine, 1050 Brussels, Belgium

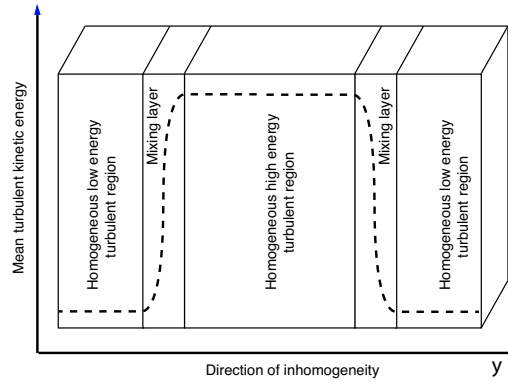


FIGURE 1. Graphical representation of the shear-free mixing layer

the shear-free mixing layer. In that respect, the creation of a DNS database at higher Reynolds number is necessary in order to make meaningful LES assessments. From the point of view of LES, the shear-free mixing-layer is interesting since it allows one to test how traditional LES models perform in the presence of an inhomogeneity without having to deal with difficult numerical issues. Indeed, as argued in Briggs *et al.* (1996), it is possible to use a spectral code to study the shear-free mixing layer and one can thus focus on the accuracy of the modelling while avoiding contamination of the results by commutation errors etc.

This paper is organized as follows. First we detail the initialization procedure used in the simulation. Since the flow is not statistically stationary, this initialization procedure has a fairly strong influence on the evolution. Although we will focus here on the shear-free mixing layer, the method proposed in the present work can easily be used for other flows with one inhomogeneous direction. The next section of the article is devoted to the description of the DNS. All the relevant parameters are listed and comparison with the Veeravalli & Warhaft (1989) experiment is performed. The section on the LES of the shear-free mixing layer follows. A detailed comparison between the filtered DNS data and the LES predictions is presented. It is shown that simple eddy viscosity models perform very well for the present test case, most probably because the flow seems to be almost isotropic in the small-scale range that is not resolved by the LES.

## 2. Initialization of the flow

From the numerical point of view, one of the most appealing properties of the shear-free mixing layer is the possibility of simulating this flow with a purely spectral three dimensional code. Indeed, periodicity can be enforced by considering a second mixing-layer, which performs the ‘reverse’ transition compared to the first one. The situation is depicted in Fig. 1. This also has the advantage that results gathered from the two mixing layers can be averaged to improve the statistics. This possibility will be systematically exploited in the presentation of numerical results in the following sections.

Given a 3D spectral code, the non-trivial part of the simulation is then to build a suitable initial condition that mimics the mixing layer. Indeed, because the decaying mixing layer is not statistically stationary, it is not acceptable to wait until the initial condition is forgotten by the flow due to the stochastic nature of turbulence. Indeed, the simulation will remain quite strongly influenced by the initial state of the velocity

field. To proceed, it is necessary to introduce a few definitions and notations. The Fourier modes associated with the velocity field  $u_i(x, y, z)$  will be denoted  $\tilde{u}_i(k_x, k_y, k_z)$  and are defined by

$$\tilde{u}_i(k_x, k_y, k_z) = \sum_{\mathbf{x}} u_i(x, y, z) e^{-i\mathbf{k}\cdot\mathbf{x}}. \quad (2.1)$$

Since the mixing layer is homogeneous in two directions it is also convenient to consider 2D Fourier transforms. Here we take the  $y$  direction as the inhomogeneous direction and define the 2D Fourier modes  $\tilde{u}_i(k_x, y, k_z)$  by

$$\tilde{u}_i(k_x, y, k_z) = \sum_{\mathbf{x}_\perp} u_i(x, y, z) e^{-i\mathbf{k}_\perp \cdot \mathbf{x}_\perp}, \quad (2.2)$$

where  $\mathbf{x}_\perp = (x, z)$  and  $\mathbf{k}_\perp = (k_x, k_z)$ . For convenience, we will also adopt the following notations:  $u_x \equiv u$ ,  $u_y \equiv v$  and  $u_z \equiv w$ . When the flow is homogeneous and isotropic, a common way to initialize the modes  $\tilde{u}_i(k_x, k_y, k_z)$  is to fix their amplitudes to match a given energy spectra  $E(k)$  and assign them random phases in such a way that continuity is enforced (Rogallo 1981). One then has,

$$\langle |\tilde{u}_i(k_x, k_y, k_z)|^2 \rangle = A^2(k), \quad \text{with } E(k) = 2\pi k^2 A^2(k) \quad (2.3)$$

and  $k^2 = k_x^2 + k_y^2 + k_z^2$ . For the case at hand, we can adopt a similar strategy but consider instead the 2D spectra in each plane perpendicular to the direction of inhomogeneity. Indeed, in those planes the flow is assumed to be homogeneous and isotropic. We thus initialize our flow by imposing the following constraints on the 2D Fourier modes (the assignment of the random phases and the treatment of continuity will be described below),

$$\langle |\tilde{u}_i(k_x, y, k_z)|^2 \rangle = B^2(k_\perp, y), \quad \text{with } E(k_\perp, y) = \pi k_\perp B^2(k_\perp, y) \quad (2.4)$$

and  $k_\perp^2 = k_x^2 + k_z^2$ . In the above equation,  $E(k_\perp, y)$  is the energy spectra of velocity field in  $(x, z)$  plane. The arbitrary part remaining is the choice of the function  $B^2(k_\perp, y)$ . For homogeneous isotropic flows, it is trivial to relate the 2D amplitudes to the 3D amplitudes (using Parseval's theorem):

$$B^2(k_\perp, y) = \int dk_y A^2(k_y^2 + k_\perp^2). \quad (2.5)$$

Note that as expected,  $B^2(k_\perp, y)$  is independent of  $y$  for homogeneous flows. In the case of the shear-free mixing layer we will choose an amplitude function  $A(k)$  for each homogeneous region and compute the corresponding functions  $B(k_\perp, y)$  using (2.5). If the 2D amplitudes functions in the high energy and low energy regions are respectively denoted  $B_H(k_\perp, y)$  and  $B_L(k_\perp, y)$ , we then define the complete 2D amplitudes function for the shear-free mixing layer as,

$$B_{ML}(k_\perp, y) = (1 - f(y))B_L(k_\perp, y) + f(y)B_H(k_\perp, y). \quad (2.6)$$

The function  $f(y)$  is equal to 0 in the low energy region and equal to 1 in the high energy region; inside the mixing layers it varies smoothly from 0 to 1. The complete initialization procedure is as follows. First we initialize our 3D Fourier modes using the procedure of Rogallo (1981). The 3D energy spectra used here is taken from the high-energy homogeneous region of the mixing layer. This ensures that the Fourier modes  $\tilde{u}_i(k_x, k_y, k_z)$  satisfy the continuity equation. The 3D Fourier modes are then transformed to  $\tilde{u}_i(k_x, y, k_z)$  using a 1D Fourier transform. At this point their 2D amplitudes are

measured and the modes are rescaled in order to match the prescribed 2D amplitudes given by (2.6):

$$\tilde{u}_i(k_x, y, k_z) \rightarrow \tilde{u}'_i(k_x, y, k_z) = \tilde{u}_i(k_x, y, k_z) \sqrt{\frac{B_{ML}(k_\perp, y)}{|\tilde{u}_i(k_x, y, k_z)|^2}}. \quad (2.7)$$

The  $\tilde{u}'_i(k_x, y, k_z)$  are then transformed back into 3D Fourier modes,  $\tilde{u}'_i(k_x, k_y, k_z)$ . By performing the transformation (2.7), one of course destroys the continuity property of the initial field and it has to be recovered by projecting the  $\tilde{u}'_i(k_x, k_y, k_z)$  onto a divergence-free field:

$$\tilde{u}'_i(k_x, k_y, k_z) \rightarrow \tilde{u}''_i(k_x, k_y, k_z) = \left( \delta_{ij} - \frac{k_i k_j}{k^2} \right) \tilde{u}'_j(k_x, k_y, k_z). \quad (2.8)$$

This in turn partly undoes the prescription of the 2D amplitudes. Fortunately, by iterating the transformations (2.7) and (2.8) one converges to a velocity field that has 2D amplitudes arbitrarily close to  $B_{ML}(k_\perp, y)$  and which satisfies continuity. At this stage, the flow still has random phases. In order to correct this problem, we have time evolved the flow until the global skewness of the velocity derivatives reached a converged value. Between each time step, the mixing layer was rebuilt using (2.7) and (2.8) in order to retain the desired 2D amplitudes profile. After that, we stopped the rebuilding procedure and let the flow decay freely.

### 3. DNS results

#### 3.1. Parameters of the simulation

The choice of parameters for the DNS was mainly guided by the following considerations. In order to have an experimental reference to compare with, the parameters of the DNS have been chosen to match as closely as possible those from the Veeravalli & Warhaft (1989) experiment performed using the 3 : 1 perforated plate. Of course, since numerical capabilities are not unlimited, some compromises had to be made. The most important restriction in the present study is the ability to adequately resolve the high-energy region of the flow. Given this constraint, the initial 3D spectra of the homogeneous high-energy region  $E_H(k)$  was chosen to match the spectra measured in the Comte-Bellot & Corrsin (1971) experiment at stage 1. This experimental spectra was fitted with the following function,

$$E_H(k) = \frac{ak^4}{(k^4 + q^4)^{1+\alpha}} e^{-bk^\beta} \quad (3.1)$$

which contains several parameters  $a$ ,  $q$ ,  $b$ ,  $\alpha$  and  $\beta$ . This fairly complicated function has been chosen because it allows an easy fit of various properties of the energy spectrum. For instance, the parameters  $b$  and  $\beta$  can be used for characterizing the viscous range of the spectrum. The parameters  $q$  and  $\alpha$  determine the energy peak and the transition between the energy containing scales and the viscous range. Finally,  $a$  determines the total energy. The function (3.1) does not allow one to derive analytical expressions for the total energy and the total dissipation in terms of the parameters  $a$ ,  $q$ ,  $b$ ,  $\alpha$  and  $\beta$ . It is thus not possible to express these parameters in terms of simple global experimental data and we have not found a systematic procedure for prescribing them. It has however been observed that the following set of parameters,  $a = 10.6$ ,  $q = 1.5$ ,  $b = 0.02$ ,  $\alpha = 1.233$ ,  $\beta = 1.1$ , allows an almost perfect fit to the Comte-Bellot & Corrsin spectrum. Of course, the value of some

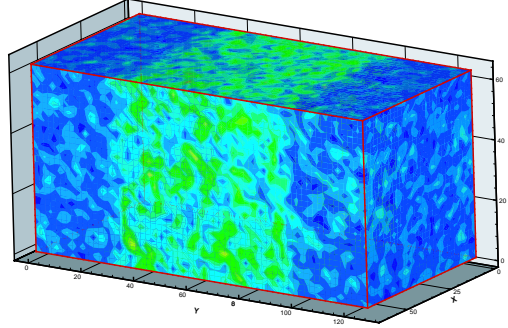


FIGURE 2. 3D contour plot of the energy density for the initial velocity field. The labels indicated on the figure correspond to grid-points. The data field was sampled every four grid-points in order to produce the graph.

of these parameters might depend on the units chosen to perform the simulation. This is not really an issue since the time scale and the length scale can be seen as entirely defined by the computational domain size  $l_x = 2\pi$ ,  $l_y = 4\pi$ ,  $l_z = 2\pi$  and by the viscosity, chosen here to have the numerical value of 0.006. In the Veeravalli & Warhaft (1989) experiment the ratio of energy between the two homogeneous regions is 6.27 while the ratio of dissipation is 7.28. These two ratios can be reproduced well by choosing the spectra of the low energy homogeneous region to be of the same form as (3.1) but with the following parameters:  $a = 2.74$ ,  $q = 3.33$ ,  $b = 0.027$ ,  $\alpha = 1.233$ ,  $\beta = 1.1$ . Furthermore, with the above choices of parameters, the maxima of the two spectra are separated by a ratio that matches the inverse ratio of the initial integral length-scales in the Veeravalli & Warhaft (1989) experiment between the low- and high-energy regions. Accordingly, the differences in typical sizes of the large-scale structures on both sides of the mixing layer are also reproduced. From these definitions it is possible to compute numerically the two functions  $B_L(k_\perp, y)$  and  $B_H(k_\perp, y)$  needed in (2.6) using (2.5). The initialization procedure is then fully defined if the smoothing function  $f(y)$  is prescribed. Here, the following choice has been adopted:

$$f(y) = \begin{cases} 0 & \text{if } 0 < y < 5l_y/24, \\ 1/2(\sin(12\pi \frac{(y-l_y/4)}{l_y}) + 1) & \text{if } 5l_y/24 < y < 7l_y/24, \\ 1 & \text{if } 7l_y/24 < y < 17l_y/24, \\ 1/2(\sin(12\pi \frac{(y-2l_y/3)}{l_y}) + 1) & \text{if } 17l_y/24 < y < 19l_y/24, \\ 0 & \text{if } 19l_y/24 < y < l_y. \end{cases} \quad (3.2)$$

With this smoothing function, the high-energy region and the combined low-energy regions have the same length. Both are five times larger than each of the two mixing layers. As an illustration, the contour plot of the initial energy density is shown in Fig. 2. As far as the numerics are concerned, our DNS was performed using a pseudo-spectral dealiased code. The grid resolution adopted consists of  $512 \times 1024 \times 512$  points. The higher resolution dimension being the direction of inhomogeneity, taken here to be  $y$ .

### 3.2. Kinetic energy diagnostics

One of the major motivations of this study is to investigate the effect of inhomogeneities on the properties of the turbulence. Since the direction of inhomogeneity is along  $y$ , it is convenient to present statistics obtained by averaging over the  $x$  and  $z$  directions.

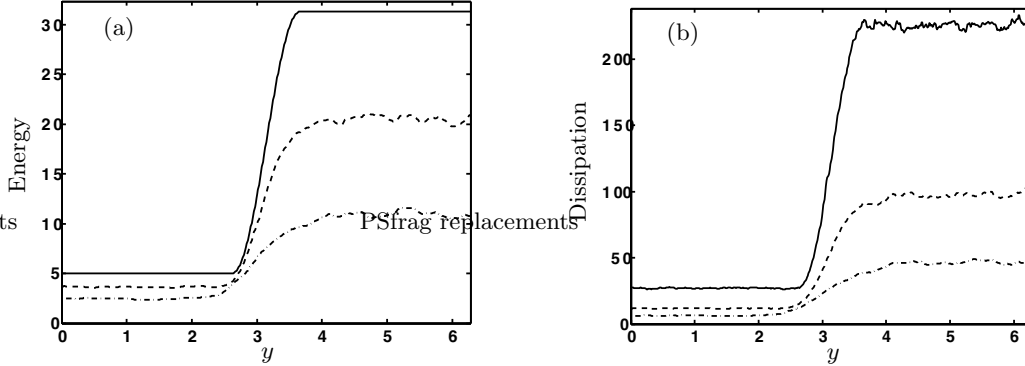


FIGURE 3. (a) Energy and (b) Dissipation rate profiles across the mixing layer calculated from (3.3) and (3.4); — :  $t^* = 0$ ; - - - :  $t^* = 0.56$ ; - · - · :  $t^* = 1.51$ .

For instance, the kinetic energy and dissipation rate profiles are calculated from the expressions:

$$E(y) = \frac{1}{2} \overline{|u_i(\mathbf{x})|^2} = \frac{1}{n_x n_z} \sum_{x,z} \frac{1}{2} |u_i(\mathbf{x})|^2, \quad (3.3)$$

$$\epsilon(y) = 2 \nu \overline{S_{ij}(\mathbf{x}) S_{ij}(\mathbf{x})}, \quad (3.4)$$

where  $S_{ij}(\mathbf{x}) = (\partial_i u_j + \partial_j u_i)/2$ . Here, and in the rest of this paper, the overbar  $\overline{\cdot}$  denotes averaging over the planes perpendicular to the direction of inhomogeneity. Figures 3(a) - 3(b) represent the profiles of the kinetic energy and the dissipation rate at three different times in the simulation. Time has been normalized using the initial eddy turnover time,  $t^* = t\epsilon_0/k_0$  where  $t$  is the dimensional time,  $k_0$  is the initial average turbulent kinetic energy and  $\epsilon_0$  is the initial average dissipation rate. The Figs. 3 demonstrate that as the decay proceeds, the mixing-layer widens but the homogeneous regions remain largely discernible. Fig. 4(a) shows the temporal decay of the average energy in the high-energy and low-energy homogeneous regions. Assuming an asymptotic power-law decay  $E(t) \sim t^n$ , a decay exponent of  $n = -1.3$  is found in the high-energy homogeneous region while in the low-energy region the decay exponent is  $n = -1.1$  (the global energy decay has a decay exponent of  $n = -1.3$ ). These decay rates are compatible with the DNS of Briggs *et al.* (1996) for which a  $k^4$  low wave-vector energy spectrum was adopted as in the present simulation. In Fig. 4(b) the 2D spectra defined in (2.4) are presented to confirm that the flow is sufficiently resolved. As was observed in Briggs *et al.* (1996), the energy of the high wave-numbers decays faster with time than the energy of the low wave-numbers. It is noted that for the discretization used and the times considered, the energy peaks remain at a constant wave-vector in the homogeneous regions. The strong influence from the homogeneous layers seems to induce a shift of this energy peak in the mixing layer towards higher wave-vectors, though this effect remains moderate for the times considered.

### 3.3. Intermittency

The skewness and kurtosis of a velocity component  $u_i$  are respectively defined as,

$$S_{u_i} = \frac{\overline{u_i^3}}{(\overline{u_i^2})^{3/2}}, \quad K_{u_i} = \frac{\overline{u_i^4}}{(\overline{u_i^2})^2}. \quad (3.5)$$

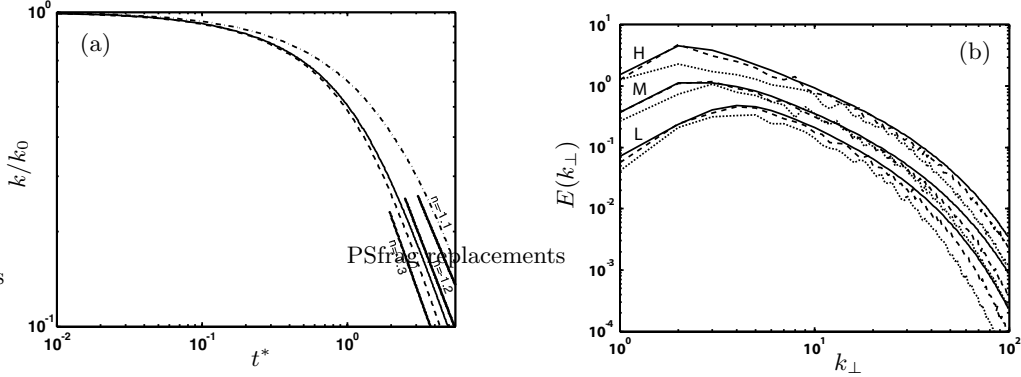


FIGURE 4. (a) Energy decays of the high (-----) and low (-.-.-) energy homogeneous regions; (—) represents the global energy decay. All curves have been normalized using their initial value of  $k_0$ . (b) 2D spectra  $E(k_{\perp}, y)$  (defined by (2.4)) computed inside the high (H) and low (L) homogeneous regions and the mixing-layer (M) for three different times; — :  $t^* = 0$ ; ----- :  $t^* = 0.56$ ; -.-.- :  $t^* = 1.51$ .

For homogeneous isotropic turbulence, measures of these quantities show that they are very close to those calculated for a Gaussian signal, i.e.,  $S = 0$  and  $K = 3$ .

The skewness profile of  $v$  is shown in Fig. 5(a). The  $y$  direction has been normalized by the half-width  $l_{1/2}$  of the mixing layer and centered around the inflection point of the variance of  $v$ . Other skewness and kurtosis diagnostics are normalized in a similar fashion (see Veeravalli & Warhaft (1989) for the details of this normalization procedure). The skewness profile of  $v$  exhibits a sharp deviation from the Gaussian value around the location of the mixing layer. As described in Veeravalli & Warhaft (1989), this behaviour is attributed to the intermittent penetration into the low-energy region of structures originating from the high-energy region (a similar penetration of structures from the low-energy region into the high-energy region is certainly also happening but is however a lot less frequent). Agreement with experimental data from Veeravalli & Warhaft (1989) is very good both in terms of the location of the peak and its amplitude. For symmetry reasons, it is expected that the skewness of  $u$  and  $w$  should remain close to zero. Up to statistical deviations, this is confirmed in our simulation (although not illustrated in this paper). Kurtosis profiles of the velocity components are shown in Fig. 5(b,c,d) and display deviations from the Gaussian value of 3 again around the location of the mixing layer. In the Kurtosis of the  $u$ , we observe an unexpectedly high peak in the profile (compared to the experimental data). At this point we attribute this issue to the fact that the profile was computed from a single realization of the flow (although averaging in the  $(x, z)$  planes was performed). We also note, however, an initial small peak in this Kurtosis component present in the initial condition (in contrast to the Kurtosis of the other two velocity components) but it is not clear whether or not it was amplified during the evolution of the flow and by what mechanism. The other two Kurtosis profiles agree very well with the experimental data again both in terms of the location of the peaks and their amplitudes. Both the numerical simulation and the experiments indicate that the deviations from the Gaussian values for  $S$  and  $K$  occur on the low energy side of the inflection points. This supports the idea that these deviations result from the more likely penetration of intermittent structures from the high-energy region into the low-energy region. Finally, it must be stressed that the initialization procedure presented in section 2, though quite sophisticated, does not allow imposition of the initial skewness or the

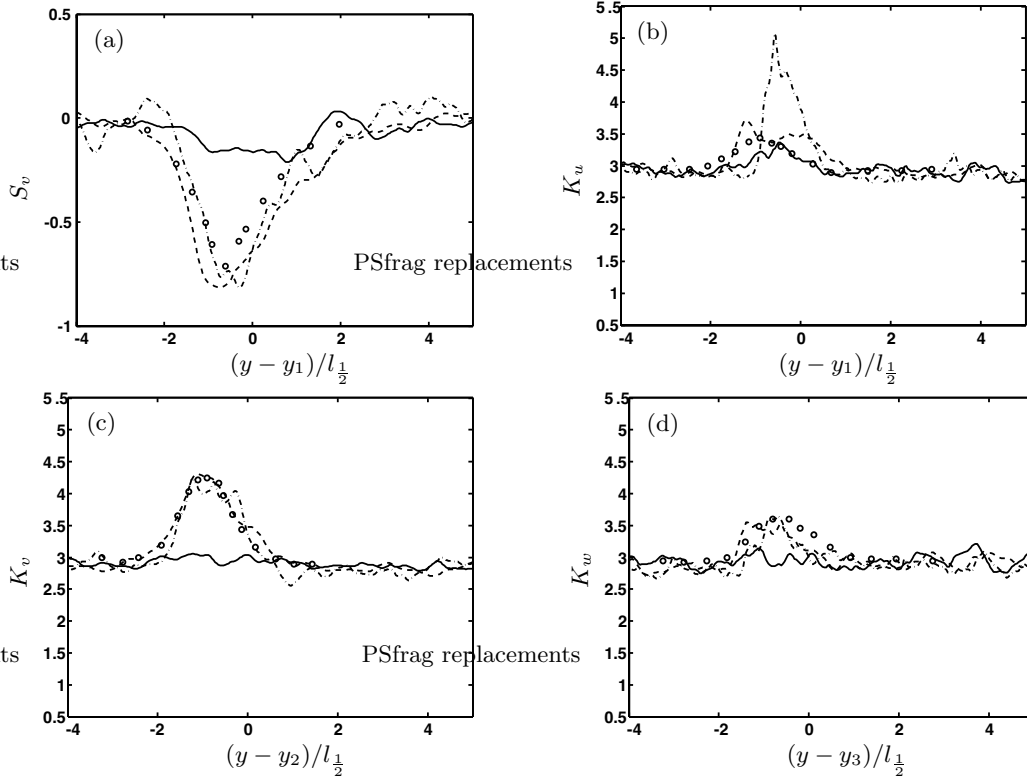


FIGURE 5. (a) Skewness of  $v$ ; (b) Kurtosis of  $u$ ; (c) Kurtosis of  $v$ ; (d) Kurtosis of  $w$ ; — :  $t^* = 0$ ; - - - :  $t^* = 0.56$ ; - · - · :  $t^* = 1.51$ ;  $\circ$ : experimental data from Veeravalli & Warhaft (1989). At  $t^* = 0$  the numerical curves are close to their Gaussian value since the penetration mechanism described in the text has not occurred yet.

kurtosis profiles in the region of the mixing layer (Gaussian values are in fact observed everywhere for the initial profiles as shown in Fig. 5 except for a small deviation for  $K_u$  as mentioned above). The fact that the DNS later reproduces the experimental profiles observed in the mixing layer indicate that the transport mechanisms are successfully resolved.

#### 4. LES of the shear-free mixing-layer

##### 4.1. Notations and conventions - LES model

Starting from the Navier-Stokes equations, one obtains the LES equations (4.1) by applying a filter, here denoted  $\widetilde{\cdot}$  (since our code is spectral, we will only consider spectral cut-offs for the LES filter):

$$\partial_t \widetilde{u}_i + \partial_j (\widetilde{u}_j \widetilde{u}_i) = -\partial_i \widetilde{p} + \nu \Delta \widetilde{u}_i - \partial_j \widetilde{\tau}_{ij}. \quad (4.1)$$

The unknown subgrid-scale stress (SGS) tensor  $\widetilde{\tau}_{ij} = \widetilde{u_i u_j} - \widetilde{u}_i \widetilde{u}_j$  needs to be modelled in terms of  $\widetilde{u}_i$  in order to close (4.1). In this work, we will use for  $\tau_{ij}$  a model proposed in Wong & Lilly (1994) and further studied in Carati *et al.* (1995) and in Dantinne *et al.* (1998). This model, which can be considered as a variant of the dynamic Smagorinsky model (Smagorinsky 1963; Germano *et al.* 1991; Lilly 1992; Germano 1992), has been

shown to perform very well in the context of homogeneous isotropic turbulence and its predictions are extremely close to the dynamic Smagorinski model. The advantage of this model rests upon the ease with which its dynamic version can be implemented. The definition of the model is the following:

$$\tilde{\tau}_{ij} - \frac{1}{3}\tilde{\tau}_{kk}\delta_{ij} = -2C\tilde{\Delta}^{\frac{4}{3}}\tilde{S}_{ij}, \quad (4.2)$$

where  $\tilde{S}_{ij} = \frac{1}{2}(\partial_i\tilde{u}_j + \partial_j\tilde{u}_i)$  is the resolved strain tensor and  $\tilde{\Delta}$  is the LES filter width. The dimensional parameter  $C$  is evaluated by introducing a second (coarser) filter  $\widehat{\cdot}$  (the test filter) and using the dynamic procedure:

$$C = \frac{1}{2(\tilde{\Delta}^{4/3} - \widehat{\Delta}^{4/3})} \times \frac{\langle \widehat{L}_{ij}\widehat{S}_{ij} \rangle}{\langle \widehat{S}_{ij}\widehat{S}_{ij} \rangle} \quad (4.3)$$

where  $\widehat{L}_{ij} = \widehat{\tilde{u}_i\tilde{u}_j} - \widehat{\tilde{u}_i}\widehat{\tilde{u}_j}$  is the Leonard tensor (note that we have systematically used the property  $\widehat{\widehat{\cdot}} \equiv \widehat{\cdot}$  valid for spectral cut-offs). As in the dynamic Smagorinski model, the only free parameter available is the ratio of the spectral cut-offs:  $\tilde{\Delta}/\widehat{\Delta}$ . In the following discussion this ratio will be assumed to be equal to 2. For homogeneous isotropic turbulence, the averages  $\langle \cdot \rangle$  in (4.3) are obtained by averaging over the whole computational domain. The idea is of course that, since turbulence is homogeneous, the constant  $C$  should be statistically independent of the position. For inhomogeneous flows in one direction, like the shear-free mixing layer or the channel flow, dependence on the direction of inhomogeneity is introduced by averaging quantities only over the other two homogeneous directions. This is justified only if the flow is not too inhomogeneous. The dynamic coefficient  $C$  then depends explicitly on the inhomogeneous direction:  $C = C(y)$ . Our LES condition was obtained by filtering (with a sharp spectral cut-off) the initial DNS field down to  $32 \times 64 \times 32$  modes. Thus, only  $\frac{1}{16}$  of the gridpoints are retained in each direction for the LES, meaning that there is one LES grid point for about 4 000 DNS grid points. The box-size is unchanged and remains  $2\pi \times 4\pi \times 2\pi$ . In our study we have also included a run obtained at LES resolution but with no subgrid-scale stress model to emphasize the effect of the model in the LES simulation. For comparison we have filtered the DNS fields stored during the simulation down to  $32 \times 64 \times 32$  modes.

#### 4.2. Comparison of the filtered DNS and the LES

Figure 6(a) represents the temporal evolution of the normalized global kinetic energy  $E/E_0$ . From the graph it is clear that the simulation with LES model does a very good job in reproducing this diagnostic, while the run with no model does not. Likewise, Figs. 6(b) and 6(c) show that the 2D spectra with LES modelling are in good agreement with DNS data. 2D spectra gathered from the run with no model exhibit a strong pile up of energy in the high wave-number side of spectra, indicating that the flow is not adequately resolved in that case.

To further illustrate the decay of the kinetic energy, we display in Fig. 7(a) and 7(b) the profiles of the kinetic energy at two different times. This is of course a more sensitive diagnostic since it retains information about the inhomogeneity of the flow. Both figures again reveal a good agreement between the DNS and LES runs and a poor behaviour of the run without modelling. Variance profiles of  $u$ ,  $v$  and  $w$  have been examined (not shown) and again the LES matches the DNS very nicely, whereas the no model simulation performs poorly. For our assessment of LES we have retained the same intermittency diagnostics described earlier: the skewness and the kurtosis of the velocity components.

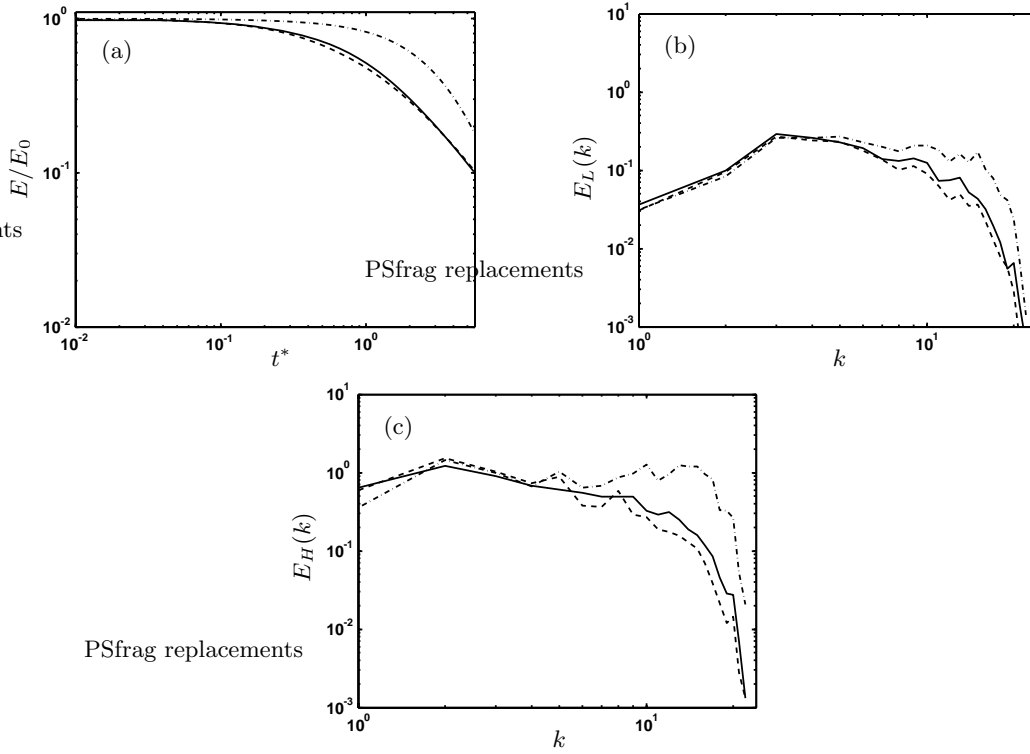


FIGURE 6. (a) Evolution with time of the normalized global kinetic energy  $E/E_0$ ; (b) and (c) 2D spectra  $E(k_{\perp}, y)$  (defined by (2.4)) computed inside the high (H) and low (L) homogeneous regions for time  $t^* = 1.51$ . In both figures, — : filtered DNS; - - - : LES; - · - · : no model.

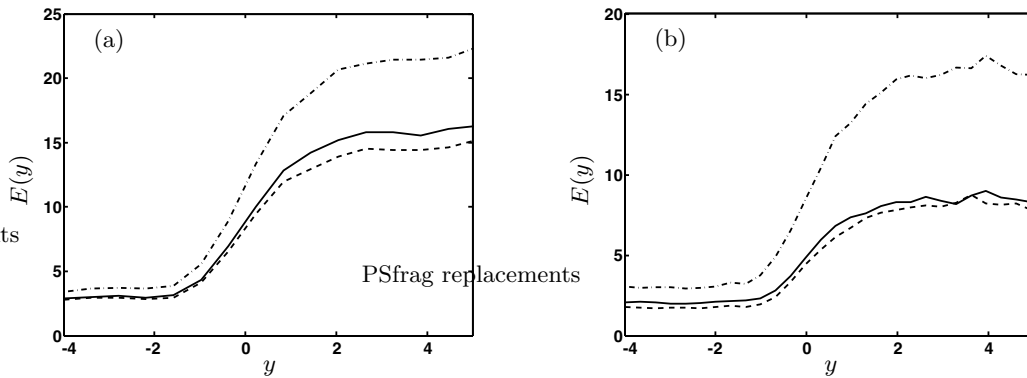


FIGURE 7. Energy profile across the mixing-layer calculated from (3.3) at times (a)  $t^* = 0.56$ , (b)  $t^* = 1.51$ . In both figures, — : filtered DNS; - - - : LES; - · - · : no model.

A sample of those quantities is displayed in Fig. 8. Once again, the LES run produces results which compare well with the filtered DNS data. Surprising at first, the run without subgrid-scale stress model also performs quite well. However, since the intermittency is attributed to large-scale structures penetrating the low energy region from the high energy region this is to be expected. Indeed, looking at the spectra displayed in Fig. 6(c),

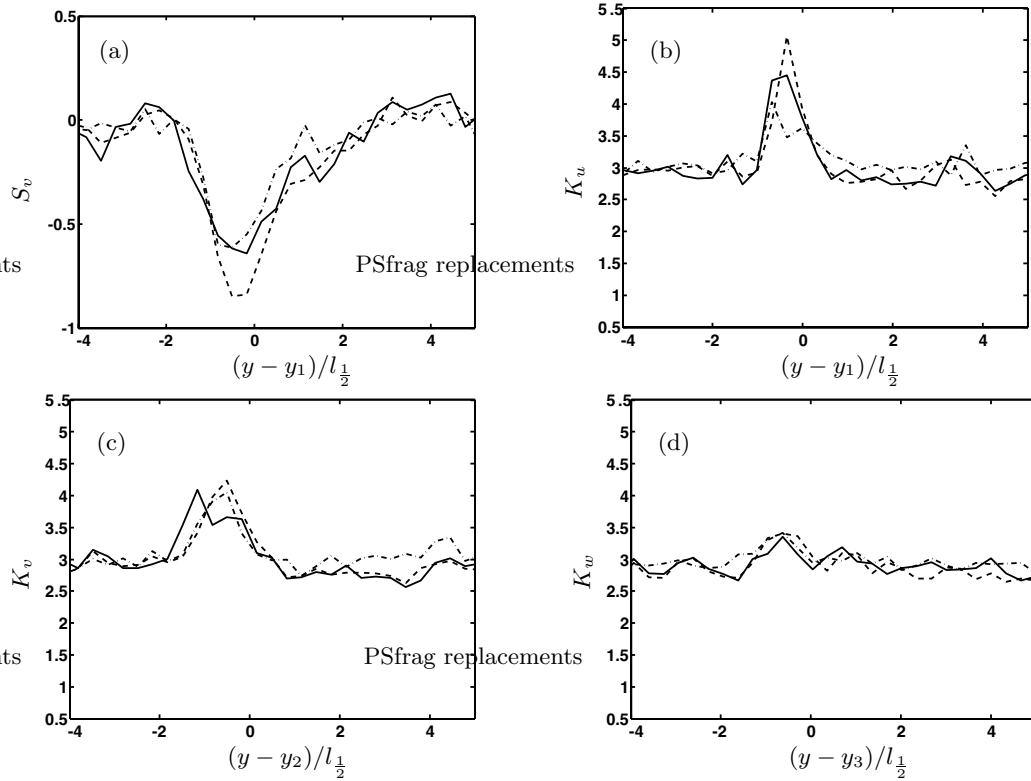


FIGURE 8. (a) Skewness of  $v$ ; (b) Kurtosis of  $u$ ; (c) Kurtosis of  $v$ ; (d) Kurtosis of  $w$ . All curves computed at  $t^* = 1.51$ . — : filtered DNS; - - - : LES; - · - : no model.

we see that the run without subgrid-scale stress model is not ill-behaved for modes at the lowest wave-numbers.

## 5. Conclusions

This study of the shear-free mixing layer reveals that DNS is capable of reproducing most of the aspects of the experimental database that have been produced by Veeravalli & Warhaft (1989). Energy, dissipation rate and velocity variance profiles are accurately reproduced. Also, departure from Gaussianity inside the mixing layer revealed by the measurement of the skewness and the kurtosis of the velocity field are also in excellent agreement with the experimental observation. This is particularly satisfactory since inside the mixing layer the initial values of these quantities cannot be prescribed by the initialization procedure and are entirely produced at later times by the transfer mechanisms simulated by the DNS. It is also observed that, in the absence of shear, no significant anisotropy is observed in this flow. This is consistent with previous numerical results and strongly supports the use of eddy-viscosity type models for the LES of such flows. As a consequence, it is not surprising that comparisons between the predictions of LES using such eddy-viscosity models and DNS show very good agreement.

### Acknowledgements

The authors are very grateful to M. Rogers and G. Burton for their comments on this manuscript. We also thank Dr. S. Veeravalli for providing us some data gathered during the Veeravalli & Warhaft (1989) experiment. B.K. and D.C. are researchers of the Fonds National pour la Recherche Scientifique (Belgium). O.D. is “boursier FRIA” (Belgium). This work has been supported by the Communauté Française de Belgique (ARC 02/07-283) and by the contract of association EURATOM - Belgian state. The content of the publication is the sole responsibility of the authors and it does not necessarily represent the views of the Commission or its services.

### REFERENCES

- BATCHELOR, G. K. 1953 *The theory of homogeneous turbulence*. Cambridge University Press.
- BRIGGS, D., FERZIGER, J., KOSEFF, J. & MONISMITH, S. 1996 Entrainment in a shear-free turbulent mixing layer. *J. Fluid Mech.* **310**, 215–241.
- CARATI, D., JANSEN, K. & LUND, T. 1995 A family of dynamic models for large-eddy simulation. In *Annual Research Briefs - 1995* (ed. P. Moin & W. Reynolds), pp. 35–40. Stanford University and NASA Ames Research Center: Center for Turbulence Research.
- COMTE-BELLOT, G. & CORRISIN, S. 1971 Simple eulerian time correlations of full- and narrow-band velocity signals in grid generated ‘isotropic’ turbulence. *J. Fluid Mech.* **48**, 273–337.
- DANTINNE, G., JEANMART, H., WINCKELMANS, G. S., LEGAT, V. & CARATI, D. 1998 Hyperviscosity and vorticity-based models for subgrid scale modeling. *Applied Scientific Research* **59**, 409–420.
- GERMANO, M. 1992 Turbulence: the filtering approach. *J. Fluid Mech.* **238**, 325–336.
- GERMANO, M., PIOMELLI, U., MOIN, P. & CABOT, W. 1991 A dynamic subgrid-scale eddy-viscosity model. *Phys. Fluids A* **3** (7), 1760–1765.
- GLIBERT, B. 1980 Diffusion mixing in grid turbulence. *J. Fluid Mech.* **100**, 349–365.
- LILLY, D. 1992 A proposed modification of the germano subgrid-scale closure method. *Phys. Fluids* **4**, 633–635.
- ROGALLO, R. 1981 Numerical experiments in homogeneous turbulence. NASA technical Memorandum 81315. NASA, Ames Research Center.
- SHEBALIN, J. V., MATTHAEUS, W. H. & MONTGOMERY, D. 1983 Anisotropy in MHD turbulence due to a mean magnetic field. *J. Plasma Phys.* **29** (3), 525–547.
- SMAGORINSKY, J. 1963 General circulation experiments with the primitive equations: 1. the basic experiment. *Month. Weather Rev.* **91**, 99–164.
- VEERAVALLI, S. & WARHAFT, Z. 1987 The interaction of two distinct turbulent velocity scales in the absence of mean shear. In *Turbulent Shear Flows 5* (ed. L. T. S. Bradbury *et al*), pp. 31–43. Springer.
- VEERAVALLI, S. & WARHAFT, Z. 1989 The shearless turbulence mixing layer. *J. Fluid Mech.* **207**, 191–229.
- WONG, V. & LILLY, D. 1994 A comparison of two subgrid closure methods for turbulent thermal convection. *Phys. Fluids* **6**, 1016–1023.